Selenite Sorption on Hydrated CEM-V/A Cement in the Presence of Steel Corrosion Products: Redox vs Non-redox Sorption

Bin Ma, Alejandro Fernandez-Martinez, Kaifeng Wang, Benoît Madé, Pierre Hénocq, Delphine Tisserand, Sarah Bureau, Laurent Charlet

Selenite sorption on hydrated CEM-V/A cement in the presence of steel corrosion products: Redox *vs.* non-redox sorption

Bin Ma[*,a,b], Alejandro Fernandez-Martinez[*,a], Kaifeng Wang[a], Benoît Madé[c], Pierre Hénocq[c], Delphine Tisserand[a], Sarah Bureau[a], Laurent Charlet[a]

[a] Univ. Grenoble Alpes, Univ. Savoie Mont Blanc, CNRS, IRD, IFSTTAR, ISTerre, 38000 Grenoble, France

[b] Laboratory for Concrete & Construction Chemistry, Swiss Federal Laboratories for Materials Science and Technology (Empa), 8600 Dübendorf, Switzerland

[c] Andra, 1/7 rue Jean Monnet, Parc de la Croix Blanche, 92298, Châtenay-Malabry Cedex, France

To ES&T

ABSTRACT

Reinforced cementitious structures in nuclear waste repositories will act as barriers that limit the mobility of radionuclides (RNs) in case of eventual leakage. CEM-V/A cement, a ternary blended cement with blast furnace slag (BFS) and fly ash (FA) could be qualified and used in French nuclear waste disposal. Chemical interactions between the cement and RNs are critical but not completely understood. Here, we combined wet chemistry methods, synchrotron-based X-ray techniques, and thermodynamic modelling to explore the redox interactions and non-redox sorption processes in simulated steel-reinforced CEM-V/A hydration systems using selenite as a molecular probe. Among all the steel corrosion products analysed, only the addition of Fe^0 can obviously enhance the reducing ability of cement towards selenite. In contrast, steel corrosion products showed stronger reducing power in the absence of cement hydrates. Selenium K-edge X-ray absorption spectroscopy (XAS) revealed that selenite uptake took place via non-redox complexation with Ca-sites and reductive precipitation of FeSe and/or Se(0). Importantly, the hydrated pristine cement showed a good reducing ability, driven by ferrous phases and (bi)sulfides (as shown by sulfur K-edge XAS) originated from BFS and FA. The overall redox potential imposed by hydrated CEM-V/A was determined, hinting to a redox shift in underground cementitious structures.

1. INTRODUCTION

Geological storage in clay-rich host rocks is foreseen in France for radioactive waste.[1, 2] In the repositories, reinforced cementitious materials are used for waste matrix, canisters, backfill, and tunnel support, which are considered as barriers inhibiting the mobility of radionuclides (RNs) in case of eventual leakage. The selection of a suitable type of cement is critical. The anticipated cement should be adequate for the subterranean work in the harsh repository environment, be friendly in CO_2 emission, and certainly be effective for RNs immobilization. CEM-V/A cement (ROMBAS, Calcia, France), a ternary blended cement consisting of 50% Portland cement (PC), 25% blast furnace slag (BFS), and 25% fly ash (FA), could be qualified and be expected to be used in French nuclear waste disposal.[3, 4]

In reinforced cementitious system, cement hydration products and the corrosion products of embedded steel are elements with the potential to immobilize RNs. The cementitious phases in hydrated CEM-V/A cement include calcium silicate hydrates (C-S-H, the major component in hydrated cement),[5] two series of aluminoferrites - ettringite[6, 7] and AFm phases,[8, 9] and portlandite. Numerous studies have reported RNs sorption behavior on cement hydration products.[10, 11] For instance, sorption of Se(IV, VI) oxyanions has attracted extensive attention as they are highly mobile and ^{79}Se ($t_{1/2}$ = 3.27(8) × 10^5 y) [12] is considered one of the few radionuclides that can dominate the ultimate biosphere exposure over geological time scales.[13] Besides, selenium is redox-sensitive and reductive precipitation into insoluble Se(0, -I, -II) is considered the most effective way to immobilize ^{79}Se.[14] Previous reports show that AFm phases are potential candidates for the retention of SeO_3^{2-}/SeO_4^{2-}.[15-17] Ettringite and C-S-H also show a good affinity to SeO_3^{2-}.[16, 17] On the other hand, corrosion of the steel embedded in the concrete could result in white rust ($Fe(OH)_2$), magnetite (Fe_3O_4), goethite (α-FeOOH), and hematite (α-Fe_2O_3),[18] going along a cross section from the inner to outer level. Fe^0 and its corrosion products can also immobilize Se(IV) through reductive precipitation and surface adsorption (inner-sphere complexation in most cases).[19, 20] Furthermore, most CEM-V/A cement probably contains Fe-(oxyhydr)oxides and metal (bi)sulfides, which originate from the blended BFS and FA, and which are effective for RNs removal. As previously reported, under acidic to slightly alkaline conditions, Fe-(bi)sulfides (e.g., pyrite,[21] pyrrhotite,[22] greigite,[14, 23] and mackinawite[24]) are able to efficiently immobilize Se(IV), resulting in Se(0), FeSe, and/or $FeSe_2$ reduction products. The way how these minerals would interact with Se(IV) after going through "*in-situ*" cement hydration is critical.

Reinforced ternary blended cement is a complex system when considered as an entire chemical barrier for RNs. Under the combined actions of various potential adsorbents, different sorption sites would compete to attract RNs, resulting in non-redox and redox sorption. In this study, we aimed to investigate the redox-sensitive RN sorption behavior in the simulated hydrated environments (hyperalkaline conditions) of reinforced blended cement by means of a combination of wet chemistry methods, synchrotron-based X-ray spectroscopic analysis, and thermodynamic modelling. SeO_3^{2-}, the analogue of $^{79}SeO_3^{2-}$, was employed as a probe molecule to detect non-redox and redox sorption sites present in hydrated CEM-V/A cement. Fe^0 and various Fe-(oxyhydr)oxides couples were introduced to simulate the presence of steel corrosion interfaces. This work provides a detailed description of the redox reaction products present in the system, and a better understanding of the redox potential imposed by the various reduced phases in the blended cement.

2. MATERIALS AND METHODS

2.1. Materials and chemicals

All the chemicals used for synthesis and stock solutions, including Fe-salts (e.g., $FeCl_2{\cdot}4H_2O$, $FeCl_3{\cdot}6H_2O$, and $Fe(NO_3)_3{\cdot}9H_2O$) and the ^{79}Se RN anionic analogue $Na_2SeO_3{\cdot}5H_2O$, were purchased from Sigma Aldrich and were analytical grade. Their containers were opened for the first time before use in the glove box. The Rombas's CEM V/A (Calcia) cement was received from French Alternative Energies and Atomic Energy Commission (CEA). It is a ternary blended cement consisting of 50% PC, 25% BFS (which may contain Cd, Cu and Fe sulfides), and 25 % FA (rich in silica and containing a small amount of Fe oxides). The resulting enhanced durability is beneficial to underground constructions in harsh environments (e.g., in geological nuclear waste repositories). A detailed chemical composition and mineralogical evolution during hydration was given in a recent study.[3] The corresponding synthetic cement pore water (CPW) and all the Fe products, including nano zero-valent iron (NZVI), magnetite, hematite, and goethite, were synthesized as described in our previous work.[20] The pH value of CPW was ~13.5 and its composition is given in Table S1. All experiments were performed in a N_2-filled glove box (O_2<2 ppm, using NaOH as the CO_2 trap) to prevent oxidation and possible CO_2 contamination. Boiled and Argon-degassed Milli-Q water (18.2 MΩ·cm) was used for all the reactions.

2.2. Preparation of hydrated Fe-bearing cement powders.

Seven types of hydrated Fe-bearing cement powders, also including the blank hydrated CEM-V/A cement (HCEM-V), were prepared. Three types among them, including NZVI-bearing cement (C-NZVI), magnetite-hematite coupling cement (C-M/H), and magnetite-goethite coupling cement (C-M/G) were produced with the aim of simulating the corroded steel interfaces in hydrated cement. The mass ratio of CEM-V/A cement powder to total Fe element content was used as 4:1, with each two Fe-(hydr)oxides pairs added in equal proportions. Three other types consisted of hydrated cement phases with the three Fe-(hydr)oxides introduced individually, named C-Mag, C-Hem, and C-Goe, respectively. Water to cement (W/C) ratio was set to 0.4 and all the components were mixed until a homogeneous samples was formed. After 2 days of cement setting, the cement paste was covered by degassed ultrapure water for 28 days. Subsequently, the cement cores were extracted, dried under vacuum to stop hydration, grinded into powder with the agate mortar, sieved through 63 μm sieves, and then stored in the glove box. All the preparation was performed under highly pure N_2 (>99.995%) protection.

2.3. Wet chemistry experiments.

HCEM-V equilibrium kinetics with CPW, sorption kinetics of SeO_3^{2-} on HCEM-V, and batch sorption of SeO_3^{2-} on all the 7 types of hydrated Fe-bearing cement particles were investigated at 25 °C in a N_2-filled glove box. An identical solid-to-liquid (S/L) ratio was fixed as 10 g L^{-1} and an initial Se concentration of 2×10^{-4} M was applied. During reaction, all the reactors were constantly placed in an end-over-end shaker. For the kinetic study, at each defined interval time, a 2 mL aliquot of suspension was sampled by filtration through a 0.22 μm pore size membrane filters. In the batch sorption experiments, Se was introduced after the cement powders were equilibrated with CPW for 2 days. After equilibrating for 30 d, the aqueous and solid phases in the batch sorption reactors were collected by membrane (0.22 μm pore size) filtration.

The total concentrations of Se, S, Ca and Fe in the filtrates were measured by inductively coupled plasma optical emission spectrometry (ICP-OES) with a Varian 720-ES apparatus after dilutions with degassed ultrapure water. The distribution ratio (R_d) of Se was then calculated (Text S1). By employing the methylene blue method,[25, 26] the total concentrations of aqueous S(-II), here called as methylene-blue-detectable sulfur (MBS), in the original filtrates were determined. To precipitate and stabilize the aqueous S(-II) the first time, a certain amount of 5 wt% zinc acetate solution was added immediately into the freshly

obtained filtrates. Sorption products from all the reactors were stored in glove box for following solid characterizations.

2.4. Selenium and sulfur K-edge XANES-EXAFS spectroscopy.

Sulfur K-edge (2474 eV) and Selenium K-edge (12658 eV) XAS experiments were conducted at the XAFS beamline of synchrotron Elettra, Basovizza, Trieste.[27] A Si(111) double-crystal monochromator was used with about 0.3 eV resolution at 2.5 keV. A silicon drift detector (KETEK GmbH AXAS-M with an area of 80 mm^2) was employed for collecting the fluorescence signal. For selenium, elemental Se foil was used for energy calibration in parallel. Elemental sulfur standard was measured and then calibrated at the beginning and the end of S K-edge experiments. All the samples for XAS were sealed using polyimide tape (double-faced sealing for selenium samples, but one-side pasting for sulfur samples), mounted on a sample holder, and measured in fluorescence mode, except for Se references, which were prepared as pellets with cellulose matrix and measured in transmission mode. Before being transferred into the vacuum experimental chamber, samples were stored under N_2 atmosphere. For EXAFS signal collection, a liquid N_2 cryostat was used to lower the temperature to 77 K, in order to minimize the effects of thermal disorder due to atomic vibrations.

Data integration and reduction of X-ray absorption near edge structure (XANES) spectra (Athena), as well as the data fitting of extended X-ray absorption fine structure (EXAFS) spectra (Artemis),[28] were performed using the Demeter software package. A linear combination fit (LCF) was applied to the Se XANES spectra to identify and quantify the selenium species. The k^3-weighted EXAFS functions of Se samples and the k^2-weighted ones of S samples were Fourier transformed (FT) in a k range 3.0-13.0 $Å^{-1}$ using a Kaiser-Bessel window. Theoretical backscattering paths were calculated by FEFF8.4,[29] to perform the fit in back-transformed reciprocal space (k).

2.5. PDF analysis.

Se(IV)-reacted Fe^0 and Fe-(hydr)oxides particles were investigated by PDF analysis of X-ray scattering. The high-energy X-ray scattering experiments were performed in beamline ID31 at the ESRF, using energy of 70.0 keV and a Perkin Elmer XRD 1621 flat detector. To avoid any oxidation, the reacted NZVI and Fe-(hydr)oxides powder samples were packed in Ø1 mm polyimide capillaries, and sealed inside capillaries by epoxy glue in glove box. These loaded capillaries were stored in anaerobic conditions until they were put on the sample racks. NIST certified CeO_2 powder sample was used for instrumental calibration and empty capillary with

the same specification for background subtraction. With collection time of 180 s, the obtained images were integrated to one-dimensional diagrams using Fit2D software.[30] PdfGetX3 code[31] was employed to transform the data into PDF patterns and calculated PDF patterns were obtained by PDFGui software.[32]

2.6. Micro-probe analysis.

In order to determine the Fe-rich phases present in hydrated cement products, the hydrated CEM-V/A cement (HCEM-V) core prepared in Section 2.2 was polished and studied by electron-probe micro-analyzer (EPMA). Regarding the sample polishing, firstly, the cured cement core was inserted in a Plexiglas container and embedded with epoxy resin. After pumping for several minutes, the cement core with epoxy resin penetrated was cured in a 50 °C oven for 24 hour. The bottom surface of the hardened sample was polished in an N_2-filled glove bag, first by silicon carbide abrasive papers, and then by different sizes of diamond pastes, going through 15 μm, 9 μm, 6 μm, 3 μm, 1 μm, and 0.25 μm under ADS lubricant in sequence. After cleaning with acetone, the sample surface was coated with 10 nm carbon film by Q150TE turbo-pumped carbon coater (Quorum technologies). Electron-probe microanalysis was performed on the JEOL JXA-8230 electron microprobe coupling with a silicon drift detector energy-dispersive spectrometer (SDD, EDS), showing the elemental distributions and fractions on selected areas or spots.

3. RESULTS AND DISCUSSION

3.1. Mineralogical compositions of hydrated cements.

XRD patterns of the synthesized Fe products are shown in Figure S1, with no impurity diffraction peak visible. Regarding the hydrated cements, XRD peak identifications were performed by comparing with PDF reference cards of major cementitious components. The crystalline phases in hydrated CEM V/A (HCEM-V) were mainly portlandite, ettringite, AFm-SO_4, calcite, mullite, and quartz, in good agreement with a previous study.[3] Among them, mullite and quartz should originate from the supplementary cementitious materials (SCMs). Besides, an amorphous phase was detected, giving a broad peak at ~13.2° 2θ. As interpreted by Claret et al,[3] the amorphous phase was not calcium silicate hydrate (C-S-H),[5] but could be ‘proto-C-S-H’. The distinction between C-S-H and the rest of the amorphous/nano-crystalline matrix is seldom made in XRD studies due to their poor crystallinity.[33] Apart from this amorphous phase, no visible peak attributed to C-S-H was observed. Regarding the hydrated Fe-bearing CEM-V/A cements, in addition to the

diffraction peaks of hydrated cement itself, the presence of corresponding iron phases also resulted in obvious diffraction peaks. In comparison to the blank hydrated cement, the corresponding amorphous phase in Fe-bearing cements showed much weaker diffraction signal, indicating that the formation of amorphous phase was largely inhibited in the presence of the nano-sized (see the morphology in Figure S2) iron phases.

3.2. S(-II) leaching kinetics and Se(IV) sorption.

Leaching kinetics of total sulfide species ([MBS], including S^{2-}, S_n^{2-}, and H_2S) from HCEM-V in the synthetic CPW was studied and the total aqueous concentrations of Ca and S were recorded (Figure S3) as well. After equilibrating with HCEM-V, ~0.4 mM more S was leached into the aqueous phase and ~30% of Ca^{2+} was adsorbed. In CPW, large amounts of Na^+ (0.076 M) and K^+ (0.211 M) exist, which could be responsible for the large STD errors of $[Ca]_{tot}$ from the ICP-OES results. With equilibrium time increasing, a considerable amount of sulfide leached out from HCEM-V. [MBS] reached the maximum value of 0.15 mM at 144 h and then decreased slightly till 0.13 mM at 160 h. Aqueous sulfide could originate from the blending BFS and its maximum concentration should be limited by the oxidants existing in HCEM-V, like Fe(III)-(oxyhydr)oxides. Sulfide is a strong reductant, even in extremely alkaline conditions (e.g., pH ~13.5 in CPW), which could be able to promote reductive precipitation of RNs.

Se(IV) sorption on HCEM-V particles was investigated by kinetics and batch sorption experiments. Concentration profiles of the kinetic experiment (Figure S4) indicated that total Ca and S concentrations kept almost constant during the reaction time. Besides, $[Se]_{tot}$ dropped rapidly from ~0.18 mM to ~0.14 mM within 24 h and then continued to decrease slowly even after 700 h. Considering that a metastable chemical equilibrium for cement hydration/degradation and RNs sorption would be even in a timescale of year,[34] we set the sorption equilibrium time at 30 days for batch experiments. The batch sorption results were shown in Table 1. After reaction, $[Ca]_{tot}$ and $[S]_{tot}$ in all the reactors stayed around 0.8 mM and 1.5 mM, respectively. Besides, all the types of hydrated cement showed good affinity to selenite, resulting in R_d values ranging from 0.038 L g^{-1} to 4.034 L g^{-1}. C-NZVI showed the strongest affinity and the largest sorption capacity (R_d ~4.034 L g^{-1}) towards selenite. As expected, the most MBS (0.0472 mM) was determined in the C-NZVI reactor, suggesting that NZVI could protect sulfide from being oxidized to some extent. For reactors containing Fe-(oxyhydr)oxides, [MBS] was nearly identical at ~0.03 mM, which was a little lower than the value in the HCEM-V reactor (~0.04 mM). Se(IV) has the potential to oxidize S(-II) into S(0)

and consequently, to be immobilized. The more reductive condition in the HCEM-V reactor compared to those with extra Fe-(oxyhydr)oxides, as indicated by the highest [MBS] value, could be partially responsible for its larger R_d value of 0.0676 L g^{-1}. Certainly, cement hydration phases (e.g., proto-C-S-H, AFm phase, and ettringite) with different proportions in different Fe-bearing cements should also contribute to the different R_d values, as these hydrates are widely considered as potential phases to remove anionic contaminants via surface adsorption and anion exchange.[16, 35, 36] In addition, comparing with the leaching kinetic experiment of HCEM-V (Figure S3), [MBS] in batch sorption experiments were generally lower probably due to the introduction of Se(IV) oxidant. In conclusion, introducing Fe-(oxyhydr)oxides into the hydrated ternary blended cement would not obviously enhance its uptake performance towards selenite, although Fe-(oxyhydr)oxides exhibited good affinity for selenite in hyperalkaline conditions via reductive immobilization and adsorption.[20] The lack of reactivity in the reactors with extra amounts of Fe-(oxyhydr)oxides could be due to the inherent existence of reducing and oxidizing Fe phases in blended cement.[37, 38] The sorbed selenium species were further identified.

Table 1. Concentrations of selected aqueous ions and the retardation factors in Se(IV) reactors with an equilibrium time of 30 days, approximately. Prior to introducing Se(IV), each type of hydrated cement equilibrated with CPW for ~ 48 h. Standard errors are given by the number in brackets on the last digit(s).

Cement type	Matrix	$[Ca]_{tot}$ /mM	$[S]_{tot}$ /mM	$[Se]_{tot}$ /mM	[MBS] /mM	R_d / L g^{-1}
-	Synthetic CPW	1.230(263)	1.510(14)	0.1789(32)	0.0002(1)	-
HCEM-V		0.787(208)	1.470(11)	0.1067(11)	0.0355(8)	0.0676(33)
C-Mag		0.789(201)	1.530(43)	0.1259(18)	0.0291(6)	0.0420(30)
C-Hem		0.747(206)	1.540(16)	0.1192(27)	0.0322(9)	0.0501(37)
C-Goe		0.804(222)	1.450(22)	0.1174(18)	0.0271(6)	0.0524(32)
C-NZVI		0.658(198)	1.620(35)	0.0043(1)	0.0472(9)	4.0346(912)
C-M/H		0.768(213)	1.560(29)	0.1247(19)	0.0335(7)	0.0435(31)
C-M/G		0.781(211)	1.700(9)	0.1296(29)	0.0333(9)	0.0380(35)

3.3. Se species from Se K-edge XANES.

Sorption products on the seven types of hydrated cement were analyzed by the LCF of Se K-edge XANES spectra (Figure 1), to identify and quantify the sorbed Se species. From the LCF results listed in Table 2, Se(IV) reduction only occurred, to a large extent, on C-NZVI, resulting in 68.1% FeSe and 6.9% Se^0. Besides, 20.5% $CaSeO_3$ contribution was quantified by LCF, probably attributed to the co-precipitation of $CaSeO_3$ or inner-sphere complexes between Ca and SeO_3^{2-}. The spectrum of C-NZVI cannot be reproduced perfectly by the three references (Figure 1a), indicating that Se(IV) could be adsorbed onto different hydrated cement products or reduced by secondary phases generated from NZVI. For HCEM-V, Se species were mainly composed of $CaSeO_3$ and Na_2SeO_3, suggesting that sorbed SeO_3^{2-} may form inner-sphere complexes (like $CaSeO_3$) and outer-sphere complexes (i.e., water-coordinated SeO_3^{2-}). For instance, sorbed SeO_3^{2-} on AFm phase may form outer-sphere complexes, having similar XANES features to Na_2SeO_3.[35] Besides, introducing a tiny amount (~0.7%) of Se^0 minimized the reduced χ square value, though this low value falls within the uncertainty range. The HCEM-V spectrum was subsequently used as a reference to perform the LCF analysis of the other cement samples. For the hydrated cement containing Fe-(oxyhydr)oxides, in addition of the largest contribution of HCEM-V reference, small percentages of $FeSeO_3$ can be added to improve the fits, indicating that selenite may complex with the Fe phases added. Besides, 3.0% Se^0 was detected in C-M/G. Indeed, the tiny amount of Se^0 identified by LCF analysis was inconclusive in the hydrated cements. However, a qualitative observation of their XANES spectra show changes at the energy position of Se^0 white-line peak that can be considered significant (see inset in Fig 1b).

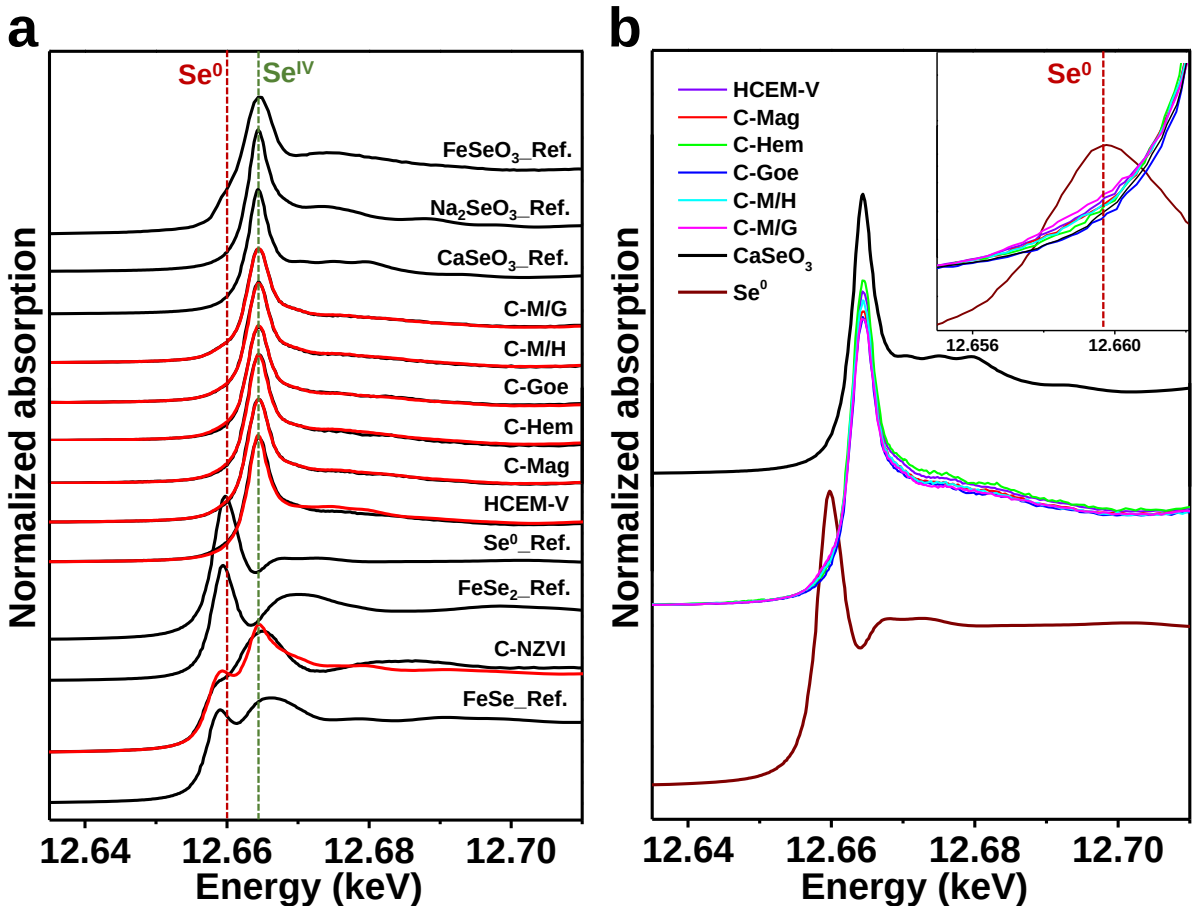

Figure 1. Se K-edge normalized XANES spectra. (a) Spectra of Se(IV) sorbed on hydrated cement with LCF results and the related Se references. (b) Normalized XANES spectra comparison of Se(IV)-sorption products and references of Se^0 and $CaSeO_3$, showing reduction of Se(IV) to Se(0). Inset is the extended XANES spectra of cement samples at the energy position of Se^0 white-line peak.

As shown in the inset of Figure 1b, the absorption intensity at the white-line peak position of Se^0 increased, indicative of the formation of Se^0. Both the spectra of C-Goe and C-Hem showed the least signal increase at ~12659.6 eV, suggesting that the Fe(III)-(oxyhydr)oxides introduced would impose oxidizing potentials, oxidize sulfide phases, and inhibit selenite reduction. Note that the intensity increase for the blank hydrated cement was even larger than that for cements with addition of magnetite, e.g., C-Mag and C-M/H. Typically, the effective reductants in the ternary blended cement could be Fe(II)-bearing phases and be sulfide phases.[37-40] To reduce Se(IV), these phases could be even more effective than the nano-sized magnetite introduced. The specific reductants at work need to be ascertained.

Table 2. LCF results of Se K-edge XANES of Se(IV)-reacted hydrated cement samples. Also reported is the concentration sum (Σ), which is not constrained to 100% for samples, and the value of the reduced χsquare (χ_ν^2), both indicating good matches to the experimental spectra.

Uncertainties are given by the number in brackets on the last digit(s), i.e., 0.7(1.7) represents 0.7 ± 1.7.

ID	FeSe (%)	$FeSe_2$ (%)	Se^0 (%)	$CaSeO_3$ (%)	Na_2SeO_3 (%)	$FeSeO_3$ (%)	HCEM-V (%)	Σ (%)	$\chi_v^2 \times 10^{-3}$
HCEM-V	-	-	0.7(1.7)	56.6(7.0)	49.3(8.4)	-	-	106.6	3.0
C-Mag	-	-	-	6.7(3.2)	-	13.2(2.5)	78.6(3.0)	98.5	0.4
C-Hem	-	-	-	22.0(4.8)	15.7(5.4)	3.5(3.7)	65.1(4.3)	106.3	1.0
C-Goe	-	-	-	2.5(3.0)	-	3.2(2.4)	87.8(2.8)	93.5	0.4
C-NZVI	68.1(4.5)	-	6.9(3.1)	20.5(1.5)	-	-	-	95.4	3.6
C-M/H	-	-	-	4.4(3.5)	-	3.8(2.7)	89.2(3.2)	97.4	0.5
C-M/G	-	-	3.0(0.4)	1.5(1.8)	-	3.2(1.4)	87.5(1.6)	95.1	0.1

3.4. Se K-edge EXAFS.

EXAFS spectra of samples HCEM-V and C-NZVI were also collected, together with some references, in order to determine the coordination environments of sorbed selenium. The k^3-weighted EXAFS oscillations (Figure 2a) showed that the two samples resulted in quite different oscillation frequencies. After Fourier transform, radial distribution functions (Figure 2b) were obtained showing the presence of multiple neighbor shells. The first neighbor shell of HCEM-V was fitted with three Se-O backscattering pairs at R = 1.69 Å and the further shells could be reproduced by each of two Se-Ca at R = 3.29 Å and 3.53 Å, respectively (Table 3). This Se complexation environment was similar to that of the $CaSeO_3$ reference, suggesting that most sorbed SeO_3^{2-} on HCEM-V may co-precipitate with Ca or structurally coordinate with Ca-sites of hydrated cement products. In contrast, most Se on C-NZVI was within reducing species, with its first shell fitted with a CN ~1.0 Se-Se pair at R = 2.37 Å and a CN ~1.4 Se-Fe pair at R = 2.39 Å. Besides, a second neighbor shell with a Se-Se backscattering pair generated from the FeSe structure was added that resulted in an improved fit. Thus, the Se coordination environment in C-NZVI can be described by that of Se^0 and FeSe, in accordance with the species distribution obtained from the XANES data. This fact leads to predict that Se removal would be controlled by co-precipitation/incorporation on Ca sites or via a reductive precipitation process, when occurring in the bare hydrated cement

phases or close to the embedded steel respectively. The presence of reduced Se in the HCEM-V sample shown by the intensity at the white line in the XANES analyses could not be ascertained in the EXAFS data, probably due to its low weight fraction.

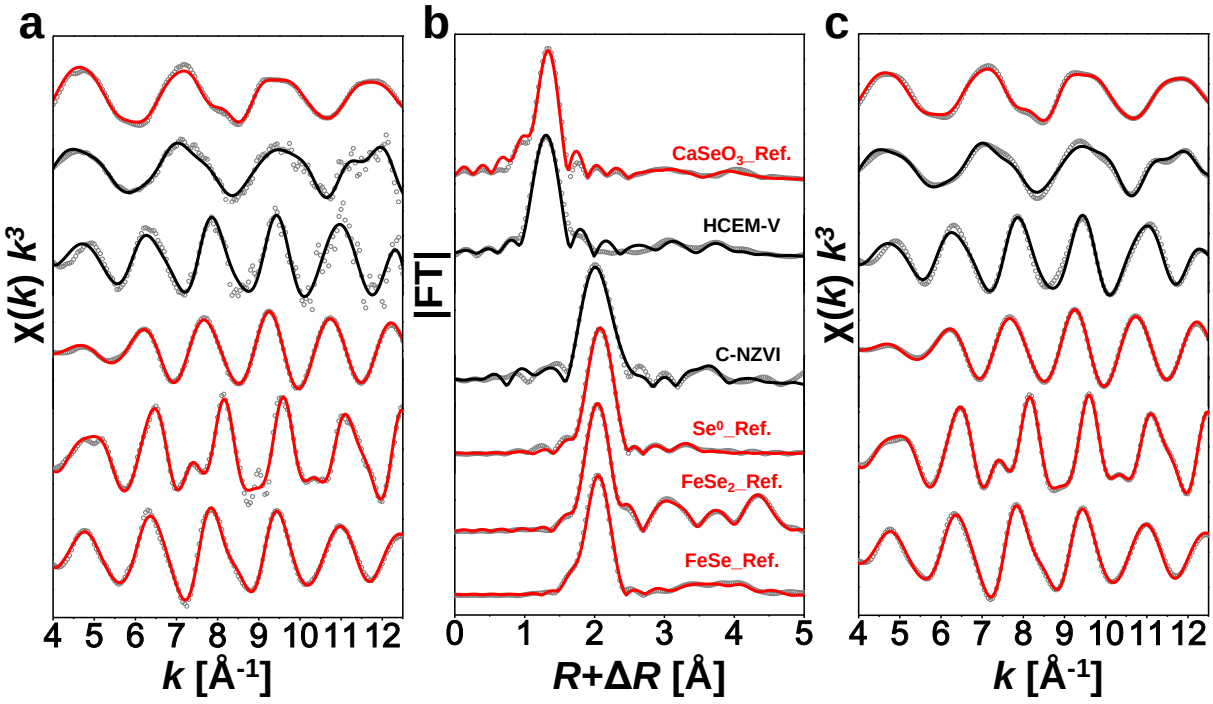

Figure 2. Experimental Se K-edge EXAFS spectra of HCEM-V and C-NZVI samples and reference compounds. (a) k^3-weighted EXAFS oscillations. (b) Fourier transformed (not corrected for phase shift) EXAFS signals. (c) Back-Fourier transformed EXAFS signal. The grey circles are the experimental data and the solid lines are fit results.

Table 3. Local structure obtained from EXAFS refinement at Se K-edge[a].

Sample	Atomic pair	CN	R (Å)	σ^2 (Å^2·10^3)	ΔE^0 (eV)	R factor %
$CaSeO_3$_Ref.	Se-O	2.9(1)	1.70(1)	1.8(3)	9.7(1.1)	4.1
	Se-Ca	1.0(5)	3.24(4)	7.8(4.6)		
	Se-Ca	1.0(5)	3.57(4)	6.7(4.8)		
FeSe_Ref.	Se-Fe	4.0(1)	2.40(1)	4.6(4)	8.6(7)	3.5
	Se-Se	7.8(2.5)	3.72(2)	9.2(5.6)		
	Se-Se	4.8(1.1)	3.94(2)	9.8(1.5)		
$FeSe_2$_Ref.	Se-Fe	3.0(1)	2.37(2)	4.4(2)	8.1(3)	1.1
	Se-Se	1.0(1)	2.56(1)	4.4(6)		
	Se-Se	4.6(8)	3.23(4)	14.1(4.4)		
	Se-Se	2.1(5)	3.35(1)	9.1(1.2)		

Se^0_Ref.	Se-Se	2.0(1)	2.37(1)	4.0(1)	6.1(8)	0.66
	Se-Se	4.3(9)	3.39(3)	14.4(2.3)		
	Se-Se	2.1(5)	3.70(3)	13.9(2.1)		
HCEM-V	Se-O	3.1(2)	1.69(2)	1.9(8)	5.4(3.4)	7.6
	Se-Ca	0.9(6)	3.29(6)	1.3(6)		
	Se-Ca	0.9(7)	3.53(6)	1.1(9)		
C-NZVI	Se-Se	1.0(3)	2.37(2)	3.3(2.5)	4.4(1.2)	8.5
	Se-Fe	1.4(3)	2.39(2)	5.1(3.1)		
	Se-Se	3.9(1.4)	3.74(1)	12.3(5.2)		
	Se-Se	2.7(1.3)	3.92(3)	5.6(2.6)		

[a] CN: coordination numbers; *R*: atomic distances; σ^2: Debye-Waller factors; ΔE^0: shift of the threshold energy; *R* factor: goodness of fit. S_0^2, 0.8950, was obtained from the experimental EXAFS fit of $CaSeO_3$ reference by fixing CN of first-shell Se-O at 3 and was applied for all the samples. Uncertainties are given by the number in brackets on the last digit(s), i.e., 7.8(4.6) represents 7.8 ± 4.6, and 2.9(1) means 2.9 ± 0.1.

3.5. Reducibility of steel corrosion products towards Se(IV).

Steel corrosion products are considered good scavengers for selenite. However, based on the above results, their addition to hydrated CEM-V/A cement did not significantly enhance the Se removal. Chemical interactions between steel corrosion products and Se(IV) in CPW were investigated, and compared with the results in the presence of hydrated CEM-V/A cement. After ~100 days of reaction, the aqueous concentrations in equilibrium were determined (see Table S2). Comparing to the cement-including cases (Table 1), the $[Se]_{tot}$ in equilibrium and R_d values in the absence of cement showed only small differences. The solid phases before and after the reaction were studied by PDF analysis. After equilibrating with aqueous Se(IV), NZVI transformed into $Fe(OH)_2$ completely due to the oxidation by Se(IV) and H_2O. Regarding M/H (Figure 3b), the correlation at ~3.50 Å decreased significantly after reaction, which corresponds to a decrease in the coordination number of the Fe-Fe scattering pair from magnetite. In the magnetite structure, the bond length of ~3.50 Å is the distance between neighboring tetrahedron and octahedron (Figure S5). In the inverse spinel structure of magnetite, all tetrahedral sites are occupied by Fe(III) and octahedral sites are occupied by both Fe(III) and Fe(II). Our results point to an oxidation of Fe(II) sites by Se(IV), leading to a change in the surface structure. A similar phenomenon was observed in the case of M/G (Figure 3c). In addition, the selenium sorbed species have been investigated in our previous work,[20] showing that at least ~50% sorbed Se(IV) was reduced under similar experimental conditions. The study indicated that both Fe(0) and magnetite still showed strong reducing ability towards Se(IV) in hyperalkaline CPW. In contrast, tiny amounts of Se(IV) were

reduced in presence of hydrated cement, although the resulting R_d values were almost the same. This suggests that the redox reactivity of steel corrosion products can be greatly suppressed due to the cement coatings. Besides, the non-redox Se(IV) sorption on hydrated cement can decrease the amount sorbed on Fe phases, weakening their chemical interactions.

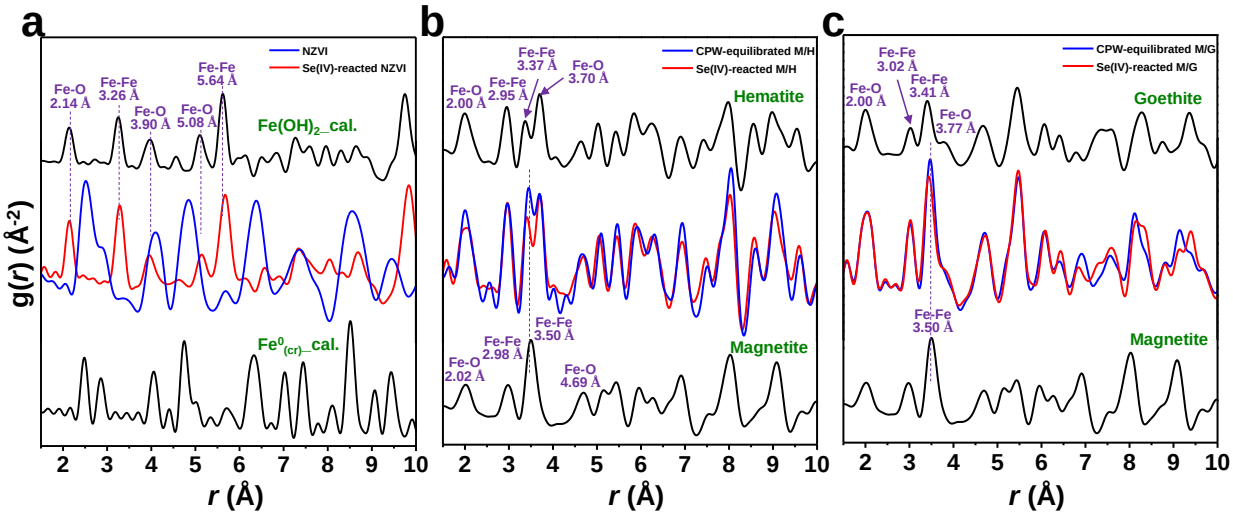

Figure 3. Experimental PDF patterns of Se(IV)-sorption products on Fe products (i.e., NZVI, M/H, and M/G) and calculated PDF patterns of the related Fe products. (a) Experimental PDF of pristine NZVI and Se(IV)-reacted NZVI; Calculated PDF references of $Fe^0_{(cr)}$ and $Fe(OH)_2$. (b) Experimental PDF of magnetite, hematite, M/H couple, and Se(IV)-reacted M/H. (c) Experimental PDF of magnetite, goethite, M/G couple, and Se(IV)-reacted M/G.

3.6. Inherent reducing power of CEM-V/A cement

3.6.1. Sulfur reducing phases

In order to ascertain the leaching source of reduced sulfur, S K-edge XAS was employed to characterize sulfur species in HCEM-V and C-NZVI. As shown in Figure 4a, their normalized XANES spectra were quite similar, possessing a main absorption peak at the energy position of sulfate white-line peak. In CEM-V/A cement, most sulfur species have +6 oxidation state, such as S(VI) in gypsum, AFm phase, and ettringite. Besides, at least two small absorption peaks can be observed at lower energies, close to feature peak energies of FeS, FeS_2, and S^0. The absorption peak at ~2471 eV can be the strong evidence for sulfide minerals. However, due to their small amount and to their different crystallinities, it was hard to identify the exact sulfide forms, e.g., Fe-sulfide or other metal (e.g., Cu and Cd) sulfides. In addition, the very close white-line peak positions of FeS_2 and S^0 increased the difficulty of ascertaining the S species attributions at ~2473 eV. Both S(-I) and S(0) species are potentially present in the

hydrated cement. The k^2-weighted EXAFS oscillations and Fourier transformed EXAFS signals of HCEM-V and C-NZVI are shown in Figure 4a/4b. Introducing NZVI did not result in an obvious difference in the sulfur spectra, indicating that Fe(0) cannot promote the formation of more sulfur reducing species by redox reactions in the hydrated cement system.

The signal oscillation frequency in k space and the signal neighbor shell at $R+\Delta R$ ~1.17 Å were attributed to the four S-O backscattering pairs (d ~1.48 Å) from SO_4^{2-}. For the second shells, the backscattering peaks were quite weak as the major sulfur form, SO_4^{2-}, mostly locates in the AFm phase and ettringite, in which SO_4^{2-} is loosely bonded in the interlayer and channels, respectively, thus receiving weak backscattering signal from further neighbor shells.[35] Signal contributions from the minor S species were not visible enough in the EXAFS spectra, but these S forms, i.e., sulfides and bisulfides, were critical for Se(IV) reduction.

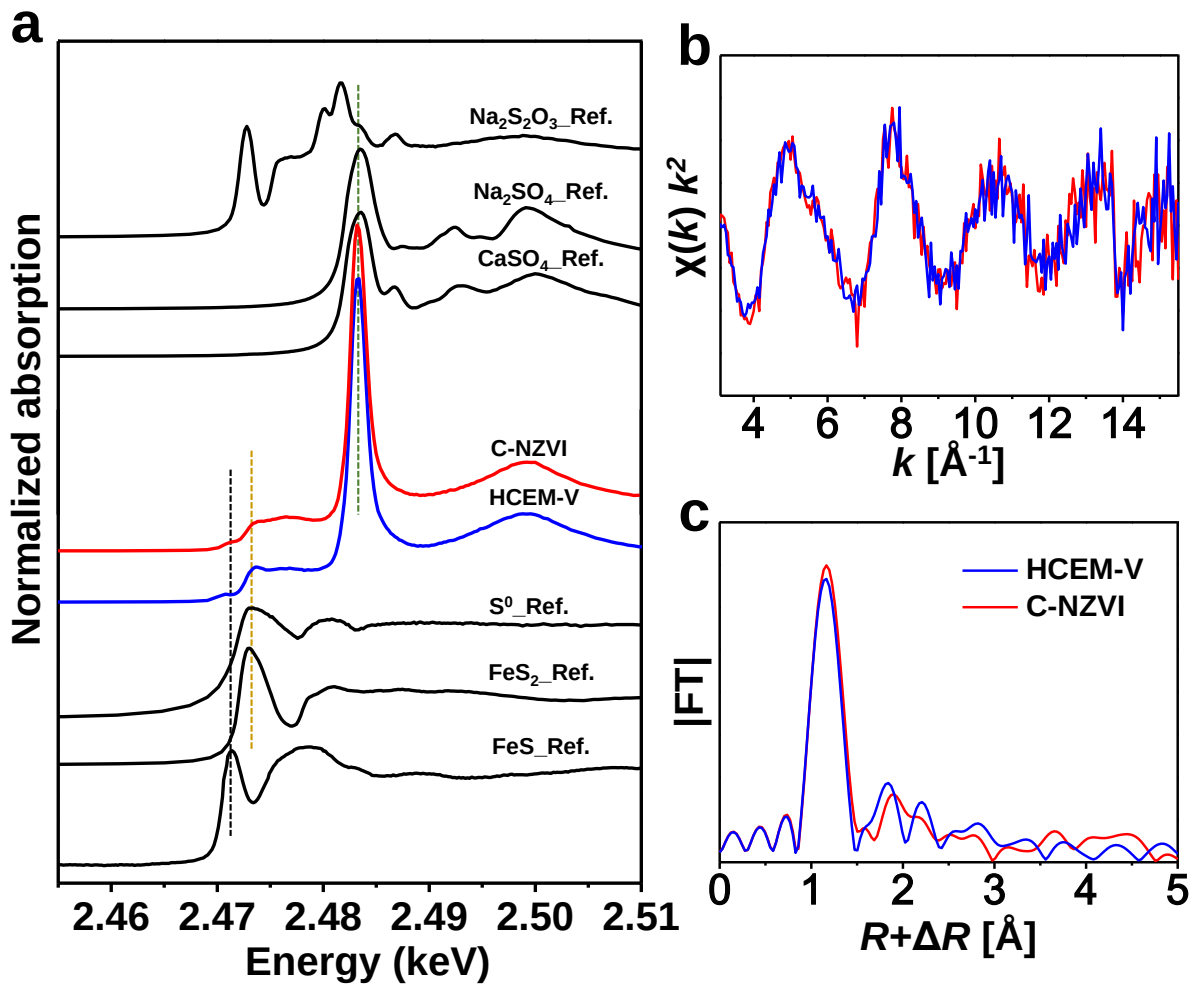

Figure 4. S K-edge XAS spectra. (a) Normalized XANES spectra of HCEM-V, C-NZVI, and related S references. (b) k^2-weighted EXAFS oscillations of HCEM-V and C-NZVI. (c) Fourier transformed (not corrected for phase shift) EXAFS signals.

3.6.2. Fe phases in HCEM-V

The polished surface of the hydrated CEM-V/A cement core was characterized by EPMA. From the backscattered electron (BE) images (Figure S6), a few bright particles with irregular or spherical shapes can be observed, indicating the existence of heavier elements. Through the EDS analysis, the heavier element was identified as Fe, with the contents reaching ~82 mol% (FeO basis). In addition, no sulfur signal detected in the bright particles suggested that the particles did not contain iron sulfide, although part of sulfides in the BFS could probably exist in Fe-bearing form. Based on the morphology of cementitious materials,[41, 42] BFS and FA can be easily distinguished. Typically, BFS grains have irregular and sharp rims while FA has consistently spherical but various sized grains. Therefore, the inherent Fe-rich phases in CEM-V/A cement can be from both BFS and FA. As widely reported, a considerable amount of Fe in BFS exists as ferrous iron [43] and the major Fe-containing phase in FA is magnetite.[39, 40] These Fe phases can contribute to the reducing capacity of CEM-V/A cement. Besides, ZVI could be introduced into BFS during ball milling.[44] However, since the reducing ability of HCEM-V was much weaker compared to C-NZVI, the ZVI could either exist in CEM-V/A cement in a tiny amount or be already corroded into Fe-(oxyhydr)oxides at the surface.

3.6.3. Possible redox reactions involving Se, Fe, and S

In steel reinforced concrete made with CEM-V/A cement, reducing Fe phases (from steel reinforcements, BFS, and FA) and sulfides (from BFS) contribute together to the reducing capacity. Aqueous sulfide species distribution was investigated as a function of pH using CPW as the matrix. As shown in Figure 5a, S^{2-} became the predominant species at pH 13.5, which would be the main S(-II) form to participate in redox reactions. ZVI can generate the lowest Eh values and thus possess the strongest reducing ability. However, the active surface of ZVI is often passivated by corrosion layers and cementitious materials, lowering its control over the Eh value that is then dominated by the products of steel corrosion. Our previous study showed that the Eh value in corroded steel system was controlled by the amorphous $Fe(OH)_2/Fe(OH)_3$ couple, resulting in a value of -456 mV at pH 13.5.[20] In spite of active ZVI surface which can even reduce H_2O to $H_{2(g)}$, the possible half-reactions involving Fe(II), S(-II), and Se(IV) are:

$$am\text{-}Fe(OH)_3 + e^- \Leftrightarrow am\text{-}Fe(OH)_2 + OH^- \quad (1)$$

$\Delta_r G^0 = 46.83$ kJ mol^{-1} $\quad Eh^0 = -486$ mV

$S^0_{(s)} + 2e^- = S^{2-}_{(aq)}$ (2)

$\Delta_r G^0 = 109.85$ kJ mol^{-1} $Eh^0 = -569$ mV

$SeO_3^{2-}{}_{(aq)} + Fe(OH)_3^- + 6e^- + 3H_2O \Leftrightarrow FeSe + 9OH^-$ (3)

$\Delta_r G^0 = 208.60$ kJ mol^{-1} $Eh^0 = -360$ mV

$2SeO_3^{2-}{}_{(aq)} + Fe(OH)_3^- + 10e^- + 6H_2O \Leftrightarrow FeSe_2 + 15OH^-$ (4)

$\Delta_r G^0 = 307.88$ kJ mol^{-1} $Eh^0 = -319$ mV

$SeO_3^{2-}{}_{(aq)} + 4e^- + 3H_2O \Leftrightarrow Se^0_{(s)} + 6OH^-$ (5)

$\Delta_r G^0 = 130.49$ kJ mol^{-1} $Eh^0 = -338$ mV

The $\Delta_f G^0$ values used were listed in Table S3. For each half-reaction, the Eh values as a function of $[S^{2-}]_{aq}$ or $[SeO_3^{2-}]_{aq}$ at pH 13.5 were calculated using the Nernst equation:

$$E_h = -\frac{\Delta_r G^0}{nF} - \frac{RT}{nF}\ln\frac{a_{Red}}{a_{Ox}} \quad (6)$$

Where R and F are the universal gas constant and Faraday constant, respectively, n is the mol number of electrons transferred, a is the chemical activity for the relevant species, and $\Delta_r G^0$ is the standard Gibbs free energy of reaction.

Generally, the oxidation of metal sulfides is controlled by two pathways, the thiosulfate and the polysulfide pathways.[14, 22] Unlike the thiosulfate pathway (for acid-insoluble pyrite), the sulfide-polysulfide-elemental sulfur pathway predominates for acid-soluble metal sulfides. As characterized by X-ray diffraction computed tomography (XRD-CT), the slag blended in CEM-V/A is more amorphous and thus contains more acid-soluble metal sulfides.[3] In the course of polysulfide oxidation, more than 90% of the sulfide in a metal sulfide can transform to S^0 as well as minor products of thiosulfate, polythionates, and sulfate. The two half-reactions of S^0/S^{2-} and SeO_3^{2-}/Se^0 were also confirmed with the experimental observation on the reaction between 0.15 mM S(-II) and 0.2 mM Se(IV) in CPW (Figure S7).

The Eh value change as a function of $[S^{2-}]_{aq}$ or $[SeO_3^{2-}]_{aq}$ for each half-reaction in CPW was plotted in Figure 5b. At the fixed pH, the *am*-$Fe(OH)_3$/*am*-$Fe(OH)_2$ half-reaction always give a Eh value of -456 mV, imposed together by all the Fe phases in reinforced concrete. The Eh curves of am-$Fe(OH)_3$/am-$Fe(OH)_2$ and S^0/S^{2-} intersected at (0.15, -456), indicating that dissolved $[S^{2-}]$ in equilibrium can only reach ~0.15 mM at -456 mV. Otherwise, the Eh values

imposed by S^0/S^{2-} would be more negative than by am-$Fe(OH)_3$/am-$Fe(OH)_2$, leading to the oxidation of S^{2-} to S^0. This is in good agreement with the S(-II) leaching kinetic study (Figure S3), showing that [MBS] reached the top at ~0.15 mM. As reported in literature, much higher $[S(-II)]_{aq}$ was released from slags into cement pore solutions, e.g., ~80 to ~110 mM [45] and ~10 mM [46] at pH ~12. Those types of slags contain less than ~1.0 wt% Fe_2O_3, while the slag in CEM-V/A ~3.3 wt% Fe_2O_3.[3] The lower $[S^{2-}]_{aq}$ in current study could be due to the higher pH values and larger portions of Fe(III) phases which originally existed in the SCMs and/or were from Fe(II) oxidations during storage. As a result, the predominant half-reaction of am-$Fe(OH)_3$/am-$Fe(OH)_2$ would limit the maximum $[S(-II)]_{aq}$. After adding SeO_3^{2-}, higher Eh values were imposed by the possible half-reactions of SeO_3^{2-}/FeSe, SeO_3^{2-}/$FeSe_2$, and SeO_3^{2-}/Se^0, leading to a lower $[S(-II)]_{aq}$ of ~0.03 mM. After 30 days reaction, $[SeO_3^{2-}]_{aq}$ decreased to ~0.10 mM, still giving a higher Eh value (-424 mV) than the intersection point (0.02, -430) of SeO_3^{2-}/FeSe and S^0/S^{2-} curves and much higher Eh values from half-reactions of SeO_3^{2-}/$FeSe_2$ and SeO_3^{2-}/Se^0. This indicated that the redox reactions between Se(IV), S(-II), and Fe(II) have not reached equilibrium after 30 days and more Se(IV) should be reduced with longer reaction time.

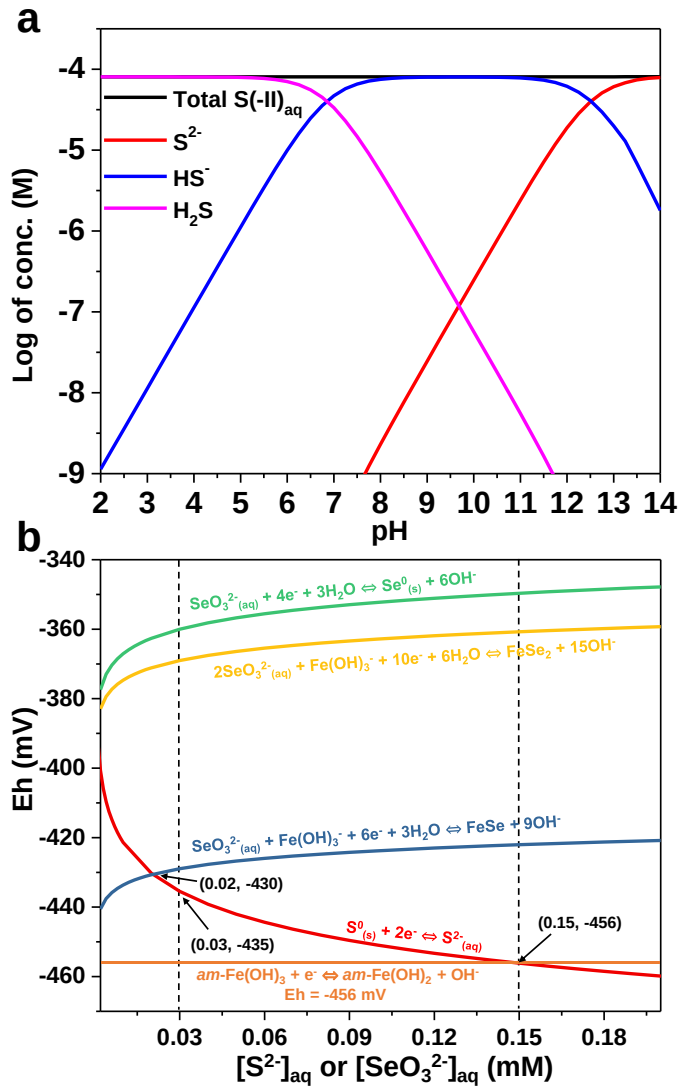

Figure 5. (a) Aqueous S(-II) speciation distribution as functions of pH. Calculations were performed by PHREEQC [47] using the Lawrence Livermore National Laboratory (LLNL) database. [S(-II)] = 10^{-4} M, the matrix was CPW. **(b)** Redox potential change of each selected half-reaction as a function of $[S^{2-}]_{aq}$ or $[SeO_3^{2-}]_{aq}$ at pH 13.5. $Fe(OH)_3^-$ concentration was set as 5 ppb, i.e., 10^{-7} M.

3.7. Environmental implications

Considering that, reductive precipitation is one of the critical retardation pathways for redox-sensitive RNs, especially for anionic RNs that are more soluble and thus mobile in alkaline conditions, reinforced cementitious structures designed for underground nuclear waste repositories should retain a certain reducing capacity. Satisfyingly, hydrated CEM-V/A cement itself shows a reducing ability towards selenite even after a relatively short interaction period (~30 days) compared with the geologic time scales considered in nuclear waste

disposal concepts. Obviously, cement hydration phases contributed the major retention capacity for selenite and immobilized the RN analogue via non-redox reactions according to the LCF analysis of XANES data. However, for a longer-term interaction, reductive immobilization would have a more critical role for redox-sensitive RNs. After thousands of years, hydrated PC is expected to degrade into C-S-H gel and aluminoferrite minerals and the pore solution pH to drop to 11 or even lower.[48] Therefore, more reducing entities, e.g., Fe^{2+} and HS^-, could leach out from the cement and participate in redox reactions.

The chemical role of steel reinforcement was simulated by introducing various Fe-(oxyhyr)oxides, their redox couples, and Fe^0 before cement hydration. Results showed that only Fe^0 can largely promote Se(IV) reduction and magnetite and Fe-couples have almost no effect on the reduction. In contrast, introducing only Fe(III)-(oxyhyr)oxides weakened Se(IV) reduction as the Fe(III) phases could oxidize the stronger sulfide reductants. This indicates that in the PC-BFS-FA ternary blended cement the active reducing interfaces could be controlled by the passivated iron, i.e., Fe(II)/Fe(III) interface,[20] and by the sulfides. Their oxidation-reduction relationship was shown in Figure 5b. The resulting redox potential should be weighted by their relative predominance. If sulfides predominates over Fe-(oxyhyr)oxides, a considerable amount of aqueous S(-II) can be released and the Eh could reach a value lower than -456 mV at pH 13.5. Since *am*-$Fe(OH)_3$ can limit $[S^{2-}]_{aq}$ to a very low value via oxidation, ~0.15 mM, we generally consider that their reducing ability is in the order of Fe^0>S^{2-}>*am*-$Fe(OH)_2$. Besides, Fe^0 is not able to reduce SO_4^{2-} into lower valent sulfur species in CPW, as confirmed by S K-edge EXAFS.

The redox potential imposed by our studied blended cement is likely to be controlled by the *am*-$Fe(OH)_3$/*am*-$Fe(OH)_2$ couple, giving a theoretical value of -456 mV. The presence of sulfides had a negligible effect over the Eh due to its lower presence as compared to Fe-(oxyhyr)oxides. The embedment of steel (Fe^0) should increase the total reducing capacity of reinforced cementitious materials. However, their apparent reducing force with respect to RNs will most probably not increase consequently, as the steel surface is always passivated and then corroded into Fe-(oxyhyr)oxides. The alkaline conditions in cement could slow down the steel corrosion process but should make the surface more preferentially covered by amorphous Fe(II)-/Fe(III)-(oxyhyr)oxides.[20] Therefore, the reactivity of steel could be weaker compared to sulfides that can release soluble S^{2-}.

This work could serve as a guide for cement manufacturing and SCMs selection applied for nuclear waste repositories in terms of redox potentials. For instance, introducing more sulfides in cement should provide a better reducing ability, and less exposure to the air (e.g., fresh blended cement) could be beneficial for the long-term reductive immobilization of RNs. Cement is the most widely used industrial material in the world for underground constructions. Chemical interactions between the underground concretes and their surroundings play important roles determining industrial (durability and sustainability) and environmental (contamination *vs.* remediation) issues, which can get some enlightened hints on redox and non-redox sorption sites from this study.

ASSOCIATED CONTENT

Supporting Information Available. Additional materials referenced in the text are available free of charge.

XRD patterns and FE-SEM micrographs of synthesized Fe products and hydrated cements. Kinetics of HCEM-V dissolution and Se(IV) sorption on HCEM-V. Atomistic structure of magnetite. EPMA image and EDS results of polished HCEM-V cement core. Photos of reaction products of aqueous Se(IV) and S(-II). CPW content. Aqueous results of Se(IV) sorption on Fe phases in N_2 atmosphere. List of $\Delta_f G^0$ values used.

AUTHOR INFORMATION

Corresponding Authors

*Phone: +33(0) 7 67 13 83 83. E-mail: mabinpku@gmail.com (B. MA).

Phone: +33(0) 4 76 63 51 97. E-mail: alex.fernandez-martinez@univ-grenoble-alpes.fr (A. FERNANDEZ-MARTINEZ).

Notes

The authors declare no competing financial interest.

ACKNOWLEDGMENTS

Dr. Giuliana Aquilanti is thanked for her assistance during the Se and S K-edge XAS measurements at the XAFS beamline, Elettra. Great gratitude to Dr. Nathaniel Findling and Dr. Valérie Magnin for performing XRD and EPMA measurements. This work has been supported by a grant from the French National Radioactive Waste Management Agency (Andra), with partial funding from Labex OSUG@2020 [investissements d'avenir; ANR10 LABX56]. Bin Ma also thanks the financial support from the China Scholarship Council (CSC). The synchrotron facilities ESRF (BM25A-25-01-976 and ID31) are acknowledged for the allocation of beamtime.

REFERENCES

1. Wang, L., D. Jacques, and P. De Cannière, *Effects of an alkaline plume on the Boom Clay as a potential host formation for geological disposal of radioactive waste.* External Report SCK• CEN-ER-28, SCK• CEN, Belgium, 2010.
2. Kosakowski, G. and U. Berner, *The evolution of clay rock/cement interfaces in a cementitious repository for low- and intermediate level radioactive waste.* Physics and Chemistry of the Earth, Parts A/B/C, 2013. **64**: p. 65-86.
3. Claret, F., et al., *Deciphering mineralogical changes and carbonation development during hydration and ageing of a consolidated ternary blended cement paste.* IUCrJ, 2018. **5**(2).
4. Trotignon, L., H. Peycelon, and X. Bourbon. *Performance assessment of CEM-I and CEM-V concrete engineered barriers in a clayey geological medium*. in *MIGRATION 2005, 10 international conference on chemistry and migration behaviour of actinides and fission products in the geosphere*. 2005. France.
5. Lothenbach, B. and A. Nonat, *Calcium silicate hydrates: Solid and liquid phase composition.* Cement and Concrete Research, 2015. **78**: p. 57-70.
6. Matschei, T., B. Lothenbach, and F.P. Glasser, *Thermodynamic properties of Portland cement hydrates in the system CaO–Al2O3–SiO2–CaSO4–CaCO3–H2O.* Cement and Concrete Research, 2007. **37**(10): p. 1379-1410.
7. Baur, I., et al., *Dissolution-precipitation behaviour of ettringite, monosulfate, and calcium silicate hydrate.* Cement and Concrete Research, 2004. **34**(2): p. 341-348.
8. Matschei, T., B. Lothenbach, and F.P. Glasser, *The AFm phase in Portland cement.* Cement and Concrete Research, 2007. **37**(2): p. 118-130.
9. Aimoz, L., et al., *Structural Insight into Iodide Uptake by AFm Phases.* Environmental Science & Technology, 2012. **46**(7): p. 3874-3881.
10. Evans, N.D.M., *Binding mechanisms of radionuclides to cement.* Cement and Concrete Research, 2008. **38**(4): p. 543-553.

11. Ma, B., et al., *A review of the retention mechanisms of redox-sensitive radionuclides in multi-barrier systems.* Applied Geochemistry, 2019. **100**: p. 414-431.
12. Jorg, G., et al., *Preparation of radiochemically pure (79)Se and highly precise determination of its half-life.* Applied Radiation and Isotopes, 2010. **68**(12): p. 2339-2351.
13. Grambow, B., *Mobile fission and activation products in nuclear waste disposal.* Journal of Contaminant Hydrology, 2008. **102**(3–4): p. 180-186.
14. Charlet, L., et al., *Nanocomposite Pyrite-Greigite Reactivity toward Se(IV)/Se(VI).* Environmental Science & Technology, 2012. **46**(9): p. 4869-4876.
15. Wu, Y., et al., *Effective removal of selenate from aqueous solutions by the Friedel phase.* Journal of Hazardous Materials, 2010. **176**(1–3): p. 193-198.
16. Baur, I. and C.A. Johnson, *Sorption of Selenite and Selenate to Cement Minerals.* Environmental Science & Technology, 2003. **37**(15): p. 3442-3447.
17. Bonhoure, I., et al., *Uptake of Se(IV/VI) oxyanions by hardened cement paste and cement minerals: An X-ray absorption spectroscopy study.* Cement and Concrete Research, 2006. **36**(1): p. 91-98.
18. Antunes, R.A., I. Costa, and D.L.A.d. Faria, *Characterization of corrosion products formed on steels in the first months of atmospheric exposure.* Materials Research, 2003. **6**: p. 403-408.
19. Fernandez-Martinez, A. and L. Charlet, *Selenium environmental cycling and bioavailability: a structural chemist point of view.* Reviews in Environmental Science and Bio/Technology, 2009. **8**(1): p. 81-110.
20. Ma, B., et al., *XANES-Based Determination of Redox Potentials Imposed by Steel Corrosion Products in Cement-Based Media.* Environmental Science & Technology, 2018. **52**(20): p. 11931-11940.
21. Kang, M.L., et al., *Effect of pH on Aqueous Se(IV) Reduction by Pyrite.* Environmental Science & Technology, 2011. **45**(7): p. 2704-2710.
22. Ma, B., et al., *The reductive immobilization of aqueous Se(IV) by natural pyrrhotite.* Journal of Hazardous Materials, 2014. **276**(0): p. 422-432.
23. Kang, M., et al., *The influence of pH and reaction time on the formation of FeSe2 upon selenite reduction by nano-sized pyrite-greigite.* Radiochimica Acta, 2016. **104**(9): p. 649-656.
24. Scheinost, A.C., et al., *X-ray absorption and photoelectron spectroscopy investigation of selenite reduction by Fe-II-bearing minerals.* Journal of Contaminant Hydrology, 2008. **102**(3-4): p. 228-245.
25. Wan, M., et al., *Occurrence of Surface Polysulfides during the Interaction between Ferric (Hydr)Oxides and Aqueous Sulfide.* Environmental Science & Technology, 2014. **48**(9): p. 5076-5084.
26. Mylon, S.E. and G. Benoit, *Subnanomolar Detection of Acid-Labile Sulfides by the Classical Methylene Blue Method Coupled to HPLC.* Environmental Science & Technology, 2001. **35**(22): p. 4544-4548.
27. Aquilanti, G., et al., *Operando characterization of batteries using x-ray absorption spectroscopy: advances at the beamline XAFS at synchrotron Elettra.* Journal of Physics D: Applied Physics, 2017. **50**(7): p. 074001.
28. Ravel, B. and M. Newville, *ATHENA, ARTEMIS, HEPHAESTUS: data analysis for X-ray absorption spectroscopy using IFEFFIT.* Journal of Synchrotron Radiation, 2005. **12**(4): p. 537-541.
29. Ankudinov, A., A. Nesvizhskii, and J. Rehr, *Dynamic screening effects in x-ray absorption spectra.* Physical Review B, 2003. **67**(11): p. 115120.

30. Hammersley, A.P., et al., *Two-dimensional detector software: From real detector to idealised image or two-theta scan.* High Pressure Research, 1996. **14**(4-6): p. 235-248.
31. Juhas, P., et al., *PDFgetX3: a rapid and highly automatable program for processing powder diffraction data into total scattering pair distribution functions.* Journal of Applied Crystallography, 2013. **46**(2): p. 560-566.
32. Farrow, C., et al., *PDFfit2 and PDFgui: computer programs for studying nanostructure in crystals.* Journal of Physics: Condensed Matter, 2007. **19**(33): p. 335219.
33. Scrivener, K.L., et al., *Quantitative study of Portland cement hydration by X-ray diffraction/Rietveld analysis and independent methods.* Cement and Concrete Research, 2004. **34**(9): p. 1541-1547.
34. Ochs, *Radionuclide and Metal Sorption on Cement and Concrete.* Topics in Safety Risk Reliability & Quality, 2016.
35. Ma, B., et al., *Selenite Uptake by Ca–Al LDH: A Description of Intercalated Anion Coordination Geometries.* Environmental Science & Technology, 2018. **52**(3): p. 1624-1632.
36. Ma, B., et al., *Evidence of Multiple Sorption Modes in Layered Double Hydroxides Using Mo As Structural Probe.* Environmental Science & Technology, 2017. **51**(10): p. 5531-5540.
37. Simon, S., et al., *The fate of iron during the alkali-activation of synthetic (CaO-)FeOx-SiO2 slags: An Fe K-edge XANES study.* Journal of the American Ceramic Society, 2018. **101**(5): p. 2107-2118.
38. Peys, A., et al., *Molecular structure of CaO–FeOx–SiO2 glassy slags and resultant inorganic polymer binders.* Journal of the American Ceramic Society, 2018. **101**(12): p. 5846-5857.
39. Valeev, D., A. Mikhailova, and A. Atmadzhidi, *Kinetics of Iron Extraction from Coal Fly Ash by Hydrochloric Acid Leaching.* Metals, 2018. **8**(7): p. 533.
40. Chen, H., et al., *Coal Fly Ash as a Source of Iron in Atmospheric Dust.* Environmental Science & Technology, 2012. **46**(4): p. 2112-2120.
41. Scrivener, K., R. Snellings, and B. Lothenbach, *A practical guide to microstructural analysis of cementitious materials*. 2018: Crc Press.
42. Lothenbach, B., K. Scrivener, and R.D. Hooton, *Supplementary cementitious materials.* Cement and Concrete Research, 2011. **41**(12): p. 1244-1256.
43. Piatak, N.M., M.B. Parsons, and R.R. Seal, *Characteristics and environmental aspects of slag: A review.* Applied Geochemistry, 2015. **57**: p. 236-266.
44. Haha, M.B., et al., *Influence of slag chemistry on the hydration of alkali-activated blast-furnace slag — Part II: Effect of Al2O3.* Cement and Concrete Research, 2012. **42**(1): p. 74-83.
45. Gruskovnjak, A., et al., *Hydration mechanisms of super sulphated slag cement.* Cement and Concrete Research, 2008. **38**(7): p. 983-992.
46. Lothenbach, B., et al., *Hydration of a low-alkali CEM III/B–SiO2 cement (LAC).* Cement and Concrete Research, 2012. **42**(2): p. 410-423.
47. Parkhurst, D.L. and C. Appelo, *Description of input and examples for PHREEQC version 3: a computer program for speciation, batch-reaction, one-dimensional transport, and inverse geochemical calculations*, 2013, US Geological Survey.
48. Lothenbach, B., E. Bernard, and U. Mäder, *Zeolite formation in the presence of cement hydrates and albite.* Physics and Chemistry of the Earth, Parts A/B/C, 2017. **99**: p. 77-94.